Article

Infrared Hyperspectral and Ultraviolet Remote Measurements of Volcanic Gas Plume at MT Etna during IMAGETNA Campaign

Nathalie Huret [1],*, Charlotte Segonne [1], Sébastien Payan [2], Giuseppe Salerno [3], Valéry Catoire [1], Yann Ferrec [4], Tjarda Roberts [1], Armande Pola Fossi [5], Delphy Rodriguez [2], Laurence Croizé [4], Stéphane Chevrier [1], Stéphane Langlois [4], Alessandro La Spina [3] and Tommaso Caltabiano [3]

[1] Laboratoire de Physique et Chimie de l'Environnement et de l'Espace, Université Orléans, Centre National de la Recherche Scientifique, Centre National d'Études Spatiales, 45071 Orléans, France; charlotte.segonne@uca.fr (C.S.); valery.catoire@cnrs-orleans.fr (V.C.); tjarda.roberts@cnrs-orleans.fr (T.R.); stephane.chevrier@cnrs-orleans.fr (S.C.)
[2] Laboratoire Atmosphères Milieux Observations Spatiales/Institut Pierre Simon Laplace, Sorbonne Université, Université de Versailles Saint-Quentin-en-Yvelines, Centre National de la Recherche Scientifique, 75252 Paris, France; sebastien.payan@sorbonne-universite.fr (S.P.); Delphy.Rodriguez@latmos.ipsl.fr (D.R.)
[3] Istituto Nazionale di Geofisica e Vulcanologia – Sezione di Catania, Osservatorio Etneo, 95125 Catania, Italy; giuseppe.salerno@ingv.it (G.S.); alessandro.laspina@ingv.it (A.L.S.); tommaso.caltabiano@ingv.it (T.C.)
[4] Office National d'Études et de Recherches Aérospatiales/Département Optique et Techniques Associées, 91120 Palaiseau, France; yann.ferrec@onera.fr (Y.F.); laurence.croize@onera.fr (L.C.); stephane.langlois@onera.fr (S.L.)
[5] Thales—Land and Air Systems France, 78990 Élancourt, France; armande.pola-fossi@fr.thalesgroup.com
* Correspondence: N.Huret@opgc.fr

check for updates

Abstract: Quantification of gaseous emission fluxes from volcanoes can yield valuable insights on processes occurring in the Earth's interior as part of hazard monitoring. It is also an important task in the framework of climate change, in order to refine estimates of natural emissions. Passive open-path UltraViolet (UV) scattered observation by UV camera allows the imaging of volcanic plumes and evaluation of sulfur dioxide (SO_2) fluxes at high temporal resolution during daytime. Another technique of imaging is now available in the InfraRed (IR) spectral domain. Infrared hyperspectral imagers have the potential to overcome the boundary of daytime sampling of the UV, providing measurements also during the night and giving access simultaneously to additional relevant gas species. In this context the IMAGETNA campaign of measurements took place at Mt Etna (Italy) in June 2015. Three different IR imagers (commercial and under developments) were deployed, together with a Fourier Transform InfraRed spectrometer (FTIR) instrument, a UV camera, a Long Wavelength InfraRed (LWIR) camera and a radiometer. We present preliminary results obtained by the two IR cameras under development, and then the IR hyperspectral imager results, coming from full physics retrieval, are compared to those of the UV camera. The comparison points out an underestimation of the SO_2 Slant Column Densities (SCD) of the UV camera by a factor of 3.6. The detailed study of the retrieved SO_2 SCD highlights the promising application of IR imaging in volcanology for remotely volcanic plume gas measurements. It also provides a way to investigate uncertainties in the SO_2 SCD imaging in the UV and the IR.

Keywords: volcanic plume; hyperspectral; radiative transfer; data retrieval; remote sensing

1. Introduction

Volcanoes are a substantial source of gases and aerosols to the atmosphere. A major scientific challenge is the quantification of volcanic gas emissions for the understanding of eruptive processes and to assess the overall impact and climate change response [1–4]. It has been demonstrated that emissions of sulfur dioxide (SO_2) by volcanoes in quiescent non-eruptive stages (passive degassing) [5–9] may significantly impact the overall sulphur budget of the Earth's atmosphere compared to other natural sources or anthropogenic activities. Though passive SO_2 emission does not extend to the stratosphere domain respect to episodic SO_2 emission during eruption [10,11], this species is persistently released by volcanoes in the troposphere at different temporal and spatial variability representing a climate-forcing factor [12–14]. In addition, on open-system volcanoes, volcanic degassing exerts a first-order role in the style and timing of volcanic eruption. Changes in the flux rate or the chemical composition of gases emitted from volcanoes can accompany or precede changes in volcanic activity i.e., represent a signal of coming eruption [15,16]. This motivates the monitoring of volcanic volatile emissions at numerous volcanoes around the world [17–19]. Sulphur dioxide (SO_2) is typically one of the most abundant volatile components in volcanic plumes (after H_2O and CO_2) and its strong UltraViolet (UV) absorption band (and low abundance in the background atmosphere) allows relatively straightforward detection [20,21]. In addition, SO_2 flux is a particularly useful parameter to monitor in the volcanic environments, as it can be considered a proxy for magma flux, assuming complete exsolution of gas and lossless transport to the point of measurement [22]. Volcanic SO_2 emission rate measurements have been carried out using ground-based UV remote sensing techniques for more than 30 years, becoming a standard practice in volcanic surveillance [17,18,23]. Emission fluxes have been documented by COSPEC [24,25] and networks of ultraviolet scanner spectrometers [19,26] based on differential optical absorption spectroscopy (DOAS). Another technique is UV camera technology [27–29] that uses band-pass filters to visualize the SO_2 plume as a 2D image. UV cameras can monitor SO_2 emission flux variability at much higher frequency (~2 Hz) than COSPEC/DOAS spectrometers, but similarly are subject to uncertainties due to time-varying wind field and possible ground effects for measurements near the point of gas emission.

Volcanic ash plumes and gas composition is also detected remotely in the infrared region by open-path Fourier Transform InfraRed (FTIR) [30–33]. Thermal infrared (8 to 14 μm) offers advantages, with respect to UV, such as the possibility to observe SO_2 flux during both day and night in various configurations (absorption and emission mode). Infrared cameras using band-pass filters, like the Cyclops camera developed by Prata and Bernardo [34], can offer the possibility to detect volcanic SO_2. FTIR enables to retrieve simultaneously several volcanic species not observable by the UV, and has been applied in volcanology in absorption mode to detect volcanic gases (H_2O, CO_2, CO_2, CH_4, N_2O, HCl, HF and CO), using hot rocks or lava as source [35,36]. However, the measurement is limited to 1D (single pixel). Hyperspectral InfraRed (IR) imagers offer the potential to image SO_2 and various other gas species in 2D in emission mode during day and night.

Whilst multi-spectral and hyperspectral sensing infrared imagers have been relatively common in space satellite application [37,38] but their ground-based counterparts are not widely used, though have prospective applications in volcanology [39,40]. The suitability of multi-pixel spectroscopy and hyperspectral imaging relies on the opportunity to simultaneously measure spectral radiance disturbed by gas signatures and the background of spectral radiance. The combined advantages of spectroscopy and imaging allow the acquisition of an image in which each pixel is associated with a determined portion of the spectrum, and where each image is a two-dimensional map of concentrations of gas compounds. Hyperspectral imagers adapted and/or optimized for gas detection in the atmosphere have mainly been developed for military applications [41] and secondarily for atmosphere characterization. For example, the Gimballed Limb Observer for Radiance Imaging of the Atmosphere (GLORIA) instrument (IMK-KIT, Germany) is used for airborne or balloon-borne measurement campaigns to characterize the chemical composition (H_2O, O_3, HNO_3, CH_4, N_2O, CFC-11, CFC-12, ...) of the upper troposphere and lower stratosphere [42–44].

In this study, we used the commercial instrument Hyper-Cam Long Wavelength InfraRed (LWIR) from TELOPS Company and two multispectral IR cameras in the MidWave InfraRed (MWIR) under development at ONERA (Office National d'Etudes et de Recherches Aerospatiales) for remote observation of volcanic gas in the plume of Mt Etna. Measurements were performed side-by-side with UV imaging camera to measure SO_2 Slant Column Densities (SCDs) in the plume and to evaluate the discrepancy between measurements obtained in the IR and the UV.

The objectives of research are threefold: first is to achieve quantitative measurements of volcanic gas; second to compare the results achieved with an IR imaging system with those simultaneous measured by UV camera to explore uncertainty and to assess the suitability of the current performance of hyperspectral imaging for measuring volcanic plume gases; and third to test and quantify the performance of our hyperspectral data processing algorithm. A secondary goal of the campaign was to test new lightweight multi or hyperspectral instruments in operational conditions, in order to estimate the ability to these new instrumental concepts to deliver useful data for future campaigns.

In the following section, we present the campaign context and the characteristics of the different instruments deployed. We report preliminary results from the two IR multispectral cameras under development and make recommendations for future use. After checking the quality of the radiance spectrum obtained by Hyper-Cam LWIR hyperspectral imager by comparing with the widely used single-pixel FTIR instrument, we present the radiative transfer retrieval code and method applied to retrieve SO_2 slant column densities. We also present sensitivity tests on the IR retrieval parameters. Then, in the last part we discuss in detail the SO_2 slant column densities results obtained by the Hyper-Cam LWIR hyperspectral imager and compare them to those obtained simultaneously by the UV camera.

2. Materials and Methods

2.1. IMAGETNA Campaign

IMAGETNA campaign was carried out between 21 and 26 June 2015. Volcanic plume observations were remotely made from the Pizzi De Neri Volcano observatory located on the North side of Mt Etna at 2,850 m of altitude. Over the five days of field activity, Mt Etna was in a quiescent stage of volcanic activity. Emissions from the four summit craters of the volcano resulted in a near-source plume that was ash poor, but variable in its consistency and magnitude. Due to the wind-speed and direction on the days of field activity and the location of the sampling site, our measurements relate mainly to the volcanic plume issued from North East Craters (Figure 1). The site of measurements allowed us to image the plume almost perpendicular to the axis of the wind and from a moderately far distance of ~2 km from the main emission area such as to observe simultaneously the volcanic plume and the clear sky. This geometry configuration allows us to perform limb remote sensing measurements under a 15° angle with respect to the horizontal.

Measurements have been performed during the five days of the campaign early in the morning (starting at 6:00 Local Time) to get the maximum of thermal contrast between the plume and the clear sky and also to prevent the presence of convective clouds, which develop in the afternoon.

The first day of the campaign was dedicated to the instrumentation deployment, tests and calibration. The collection of the data was properly carried out in four days. Nevertheless, among of recorded data, some sequences were rejected due to meteorological conditions such as the sporadic presence of clouds, which induce too strong opacity for infrared remote sensing measurements but also strong winds inducing too much vibration of the instruments. Good quality measurements sequences were recorded between 25 and 26 June.
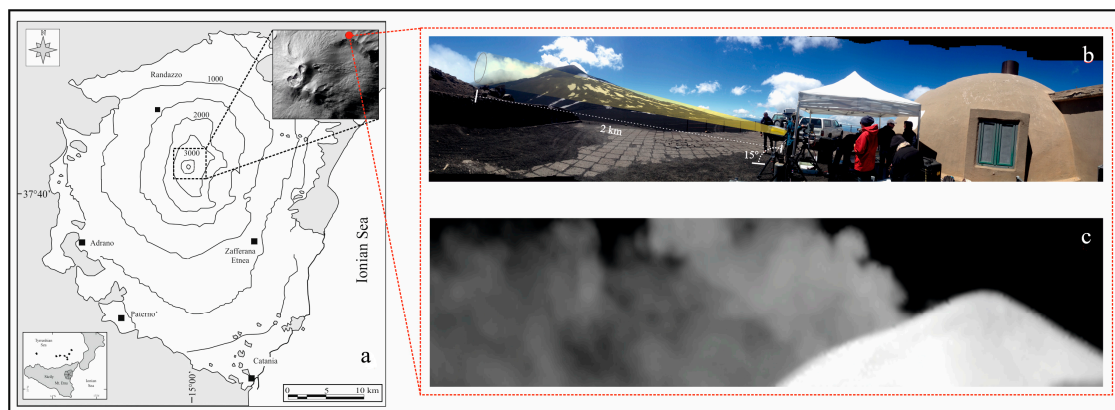
Figure 1. (**a**) Map of Mt Etna, the shaded relief on the upper right corner details the volcano summit craters and the location of the Pizzi de Neri observatory (solid red circle). In the bottom left is showed the geographic location of Mt Etna and Sicily. (**b**) Instrumental setup at the sampling locations Pizzi de Neri from which remote volcanic gases from the volcanic plume of Mt Etna were taken between 21 and 26 June 2015. (**c**) Infrared image of the volcanic plume issued from the summit North east crater of Mt Etna by Hyper-Cam Long Wavelength InfraRed (LWIR) instrument on the 26 June 2015.

Data collection was performed deploying six instruments in order to observe the gas plume using different spectral regions, at different spectral resolution, and using the properties of gas emission under limb viewing (Table 1). Three IR imagers were deployed, two of them (SIBI, which stands for "Spectro-Imageur Biréfringent" and Filament) are under development at ONERA and were deployed out of the laboratory for the first time, the third one was provided by TELOPS Company (Hyper-Cam LWIR). Together with the three IR imaging systems, measurements were also carried out by a FTIR single pixel spectrometer in emission mode (OPAG 33: Open-Path Gas Analyzer, Brucker company), which covers the entire spectral range of the different IR imagers, and a UV camera for the SO_2 measurements. Each instrument differs by the physical technology described below.

**Table 1.** Technical Characteristics of the Instruments Deployed During the IMAGETNA Campaign.

Instruments	Spectral Range (μm)	Spectral Resolution (cm^{-1}) or # of Bands	Pixel Number	Instantaneous Field of View	Reference
Spectro Imageur Biréfringent (SIBI) *Under development*	[3.7–4.8]	14	640 × 512[a]	1.6 mrad	[45]
Filament Imager *Under development*	[3–5]	24 bands	56 × 56	1.1 mrad 3.5° × 3.5°	[46] [b]
Hyper-Cam Imager Long Wavelength InfraRed (LWIR)	[7.7–11.8]	1, 2, 4, 8 and 32 during this campaign	320 × 256	1.4 mrad 25.6° × 20.4°	[47] TELOPS company
Fourier Transform InfraRed spectrometer (FTIR) *OPAG 33*	[3.5–14]	1	1	10 mrad	Bruker company
UltraViolet (UV) Camera	0.310 and 0.330	10 nm	1380 × 1040	365 μrad 28.8° × 21.9°	JAI CM-140GE-UV

[a] 640 × 512 is the raw image size, a spatial scan is necessary to measure the hyperspectral cube; [b] more and newer filters were used for the IMAGETNA Campaign then in the proceeding from Sakat et al. [46].

Both, UV camera and FTIR, were placed side-by-side to capture the entire scene allowing to complement the IR devices. We thus have the possibility to compare SO_2 Slant Column Densities (SCD) images obtained simultaneously in the IR region from Hyper-Cam LWIR and in the UV region from the UV camera.

The FTIR spectrometer and the Filament imager were set up on the same platform assuring the instruments looking at the same scene. The SIBI, the Hyper-Cam LWIR, and the UV camera instruments

were deployed close to each other looking in the same direction to cover at least a part of the same scene (Figure 2).
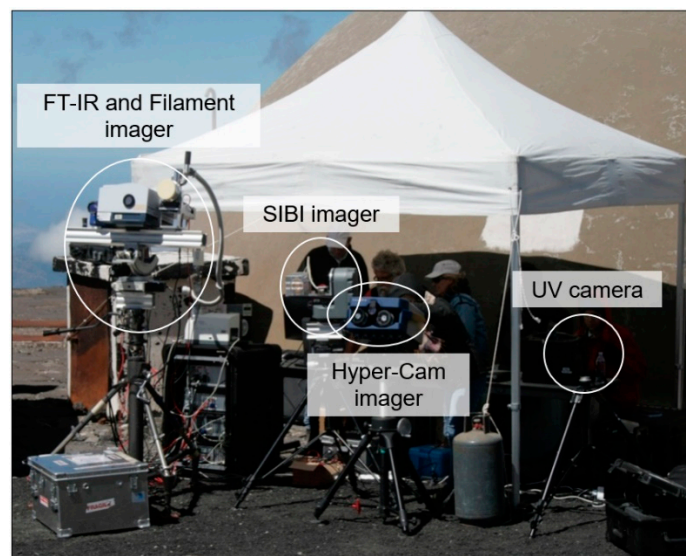
Figure 2. Setup of the instruments employed over the five days of the field campaign at Mt Etna. Remote volcanic plume observations were performed by five different devices in the InfraRed (IR) and UltraViolet (UV) region such as to evaluate the discrepancy between retrieved SO_2 Slant Column Densities (SCDs).

2.2. Lightweight SIBI Imager

SIBI, is a novel compact hyperspectral camera in the mid-IR which uses Static Fourier Transform (SFT) to produce a hyperspectral data cube with a moderate spectral resolution and a full width at half maximum (FWHM) of 14 cm^{-1}. SIBI is a very compact concept in comparison with existing hyperspectral cameras [45]. This is possible by the use of a birefringent interferometer, and a very compact cryogenic setup. SIBI camera combines a static interferometer and an imaging lens to obtain an interference pattern on each raw image. Thanks to this interference pattern and to a spatial scan of the scene through a rotation of the whole instrument, we can recover the data cube [48,49]. The size reduction of SIBI, compared to other cameras, is firstly due to the use of a birefringent interferometer, based on polarization splitting. Indeed, such an interferometer amounts to a plate merely set in front of the camera (more precisely, this plate is a stack of two parallel plates between two polarizers). The second cause of size reduction comes from the use of a very compact cryogenic camera. Details can be found in PhD manuscript of Pola Fossi [50]. A first prototype of the spectral imager ($12 \times 12 \times 20$ cm^3 and 2.7 kg) has been involved in the IMAGETNA campaign for proof of concept. It was installed on a rotation stage (Figure 2). This operation generated an interferometric cube which was post-processed through four steps to create the spectra of the points of the scene. The first step is to correct the image by subtracting the background, removing bad pixels and performing digital gain correction. Then, the optical image distortion is corrected using a pinhole camera model and homography for the camera panning distortion. A correlation algorithm is applied to register images and thus to obtain a full interferogram for each point of the scene. Spectrum is calculated by a Fourier transform from this interferogram and is radiometrically calibrated to deliver the spectral radiance at the entrance window level.

2.3. Filament Imager

Filament is a multispectral mid-IR imager. Its concept is derived from the Tombo system [51]: the pupil is divided by an array of micro-lenses, to form multiple images (which we will call "small images") of the scene on the focal plane array. Besides, a spectral filter is set on each micro-lens, so that each

small image of the scene is associated to one spectral content. We thus obtain a snapshot multispectral imager. It is a compact instrument fully cryogenic to reduce the instrumental background, currently cooled by liquid Nitrogen. The innovation in Filament lies in the spectral filters. Indeed, these filters are subwavelength gratings [52] made of narrow slits in a gold layer, deposited on a dielectric layer. Since the grating period is lower than the wavelength, the diffracted orders are evanescent, and the zero[th] order transmission is extremely low because of the reflective gold layer. However, at a specific wavelength, the first diffracted order in transmission is coupled into the waveguide formed by the dielectric layer and then re-diffracted in the zero order by the grating. Thus, the component exhibits a quite sharp transmission at this specific wavelength. Thanks to a 2D geometry for the grating, the transmitted light is unpolarized.

2.4. Hyper-Cam LWIR

2.4.1. Instrument Description

The Hyper-Cam LWIR from TELOPS Company combines an IR camera as well as a FTIR which means that for every pixel in an image we have an infrared spectrum. It provides an excellent image quality with a 320×256 pixels Focal-Plane Array (FPA) detector. An external telescope for magnification of 0.25 was added to the camera during the campaign in order to widen the field of view (FOV) by 4 ($25.6° \times 20.4°$). The Hyper-Cam LWIR offers user-selectable spectral resolution from 0.25 cm^{-1} to 150 cm^{-1}. During the campaign, we have mainly used spectral resolution of 2 and 4 cm^{-1}. A radiometric calibration was performed before and at regular intervals between measurement sequence using two black bodies at different temperatures. The black bodies temperatures must be close to the scene temperature for higher accuracy (~1 °C). Over the campaign, data were recorded selecting the temperatures of 15 and 25 °C, since the use of lower temperatures would have generated condensation on the blackbodies.

The Hyper-Cam acquisition software "Reveal Pro 5", developed by TELOPS Company, was used to record the data. Each file in a given sequence of measurement is called datacube. Datacubes, which corresponds to an IR image with an IR spectrum for each pixel, as said above, are available in raw format (interferogram) or in calibrated radiance. The acquisition time for each datacube is fully dependent on both spectral and spatial resolutions. In order to capture the plume dynamics, we've adjusted the spectral and spatial resolutions of the Hyper-Cam LWIR to get an acquisition time between 1 to 2.5 seconds per datacube.

2.4.2. Retrieval Methodology

The LATMOS Atmospheric Retrieval Algorithm (LARA) used to retrieve SO$_2$ slant column densities from Hyper-Cam LWIR instrument measurements has been developed over the past decade [53,54] (LATMOS: Laboratoire Atmosphère, Milieux, Observations Spatiales). It has been widely used to analyze atmospheric spectra recorded from ground-based, balloon or satellite-borne experiments, both in absorption or emission mode, but also for the limb or the nadir geometry: LPMA-balloon [55,56], MIPAS-Envisat satellite [57], IASI-Metop satellite [58,59]. LARA allows the simultaneous retrieval of spectra in several spectral windows for the joint retrieval of slant column densities of various species. Surface temperature and emissivity, and if needed instrumental line shape or instrumental spectral shift, may be fitted together with the species. The retrieval algorithm chooses the optimal estimation method and includes an accurate line-by-line radiative transfer model and an efficient minimization algorithm of the Levenberg-Marquardt type [60]. The full error covariance matrix is calculated within the retrieval process (measurement noise and the smoothing error as described in Rodgers, 2000 [60]). The forward model (i.e., the radiative transfer model) uses molecular parameters which are mainly extracted from the HITRAN 2012 database [61]. Individual line shapes are calculated with a Voigt profile based on the Lorentzian parameters listed in the spectroscopic database and the line shifting coefficient can be used when non-zero in HITRAN 2012. The calculation takes into account the water

vapor continuum [62] as well as water vapor self-broadening. The reflected downward flux and the reflected or diffused sunlight are modeled. For the present work, the algorithm was tailored to the specificities of Hyper-Cam LWIR spectra, Mt Etna plume characteristics and shape, and the limb geometry. As in Rix et al. [63], the plume shape is assumed with a predefined central plume height Z_{plume} and a Gaussian distribution with a half-width at half-maximum equal to plume thickness Tk_{plume}. Assumptions on the thickness of the plume and the altitude of the plume centre were made by combining visual observations and the characteristics of the relief of the Mt Etna.

The characteristics of the plume are defined according to the following 3 parameters:

1. The additional temperature inside the plume compared to ambient air $\Delta T_{plume} = 1\ K$
2. The thickness of the plume $Tk_{plume} = 400\ m$
3. The altitude of the plume centre (where gas and particulate due to Etna emission is supposed to be maximum) $Z_{plume} = 3.2\ km$

To take into account particles contribution to the IR spectrum, we parametrize that contribution considering a spectral dependency of the optical thickness (first order linear modeling) of the plume. The line of sight (limb view) considered is divided into 43 layers from the instrument altitude (2.8 km) up to the top of the atmosphere (80 km), with layers of 100 m in the plume. For each path in each layer, temperature, pressure, path length, air concentration and slant column densities (SCD) are estimated. The temperature and pressure have been derived from the combination of meteorological sounding data over Trapani performed the same day and ECMWF (European Centre of Medium-range Weather Forecast) analyses. Trapani is the closest radio-sounding station to Mt Etna.

SO_2 is retrieved in the spectral window 1,100–1,200 cm^{-1}, considering H_2O, CO_2, O_3, N_2O, CO, CH_4 and SO_2 SCDs, as well as optical thickness due to particles in the plume contributing to the IR spectrum. Particles optical thickness and SO_2 SCD are retrieved in the plume whereas all the other species are distributed on the entire slant column. It is a full physic retrieval.

For each spectrum, the following parameters have been retrieved (state vector):

*   One scaling factor for the initial profiles of each molecular species (H_2O, CO_2, O_3, N_2O, CO, and CH_4) except SO_2;
*   One scaling factor of the SO_2 Volume Mixing Ratio (VMR) in the centre of the plume (SO_2 VMR outside the plume is fixed at the climatological value), with a linear variation of the VMR from the scaling factor from the centre to the edge;
*   Two parameters to consider the spectral dependence of the optical thickness due to particles;

From these retrieved state vector variables, the slant column densities of SO_2 is then derived together with corresponding quantities like H_2O SCD. The SCDs of SO_2 are then directly comparable to other measurements (see Section 3). The quality of the retrievals is evaluated by performing χ^2 tests. A reduced χ^2 value close to 1 indicates that the residual of the retrieval is at the level of the instrumental noise.

2.5. FTIR Instrument

The FTIR is set to a spectral resolution of 0.5 cm^{-1}. The non-linearity effects are processed by the Bruker software. The raw results are used in the spectra output of the capture software. Measurements of a black body reference temperature (5 °C, 10 °C, 15 °C, 20 °C) enable radiometric calibration (linear least squares) for each wavelength. As expected for ambient temperature emitter, the resulting spectra are much more intense between 8 and 12 μm than between 3 and 5 μm. The radiometric calibration is more accurate in the (8–12) μm spectral range which allows us to compare brightness temperature (BT) spectra with those of Hyper-Cam LWIR instrument.

2.6. UV Camera

Volcanic SO_2 observations in the UV were performed by a dual-SO_2 camera system. The configuration consists of two CCD cameras (JAY CM-140GE-UV) with Sony ICX407BLA sensors (1,380 × 1,040 pixels) with sensor quantum efficiency of ~7%. The two cameras are mounted side-by-side and aligned such that they view identical scenes. Light is focused onto the sensors using 12 mm focal length quartz lenses.

Two interference band-pass optical filters, with Full Width at Half Maximum (FWHM) of 10 nm and central wavelengths of 310 and 330 nm, respectively, are installed to the lenses to enhance sensitivity to SO_2 and aerosol, and just aerosol, respectively (e.g. [64]).

Field of view is of 28.8° width × 21.9° height. The SO_2 camera is controlled by custom-built software, which manages the collection of images at a sampling rate between 0.1 and 0.03 Hz depending on scene luminosity. Shutter time is adjusted automatically to avoid over-exposure.

The system is coupled with a UV spectrometer (Ocean Optics usb2000+), which collects open-path in-plume ultraviolet spectra such as to calibrate the apparent SO_2 column amount observed by the camera system in absolute. Raw UV camera images are processed following the protocols outlined in Burton et al. [64] in which previously stored clear sky images from each camera are used to normalize the measured images from the 310 nm and 330 nm cameras, which are then divided by each other to produce an SO_2 transmittance image. After taking the negative natural logarithm of the transmittance image, it is converted in a differential optical thickness, which is then converted to SO_2 SCD by calibrating the amounts with SO_2 inverted by DOAS ultraviolet spectroscopy [26,65].

3. Results

3.1. Preliminary Results of SIBI and Filament Imagers

Figure 3 presents different data from SIBI: a raw (interferometric) image of the scene (Figure 3a), a monochromatic image at 4.8 µm (2,060 cm^{-1}) (Figure 3b), and few examples of calibrated spectra at entrance pupil plotted either in spectral radiance (Figure 3c) or in brightness temperature (Figure 3d). The noise level was estimated from the experimental hyperspectral cube to take into account both the temporal detector noise and the spatial impact of the image processing. We find a Noise Equivalent Spectral Radiance (NESR) of 11 nW/sr/cm^2/cm^{-1}, which means a Noise Equivalent Temperature Difference (NETD) of 880 mK at 2100 cm^{-1} for a blackbody at 20 °C. Although the NESR is quite constant in the 3.7–4.8 µm spectral band, the NETD increases at higher wavenumbers (lower wavelengths), as it can be seen on Figure 3d: this is due to the high dynamic of the Planck's law for ambient temperature in the MWIR (see Figure 3c).

The behavior of this very compact multi spectral IR camera was quite satisfactory [50]. However, the spectral characterization of the instrument (measurement of the map of the Optical Path Differences) was only done in the laboratory at a temperature about 20 °C, while in the field the temperature was below 10 °C. This temperature difference modified the birefringent interferometer, inducing errors on the spectral calculation (roughly, a dilatation of the spectral axis reaching few tens of cm^{-1}). Such an issue could be corrected in future experiments either by a more exhaustive characterization of the instrument in the laboratory, or by implementing a thermal control of the birefringent plate, or by performing in situ spectral calibration (with a monochromatic source).

The Filament instrument has a simpler processing chain: it consists in calibrating (as in a classical camera) each small image, taking into account its spectral sensitivity, and then in interpolating the 24 small images on a common grid, with fixed registration parameter measured in the laboratory.
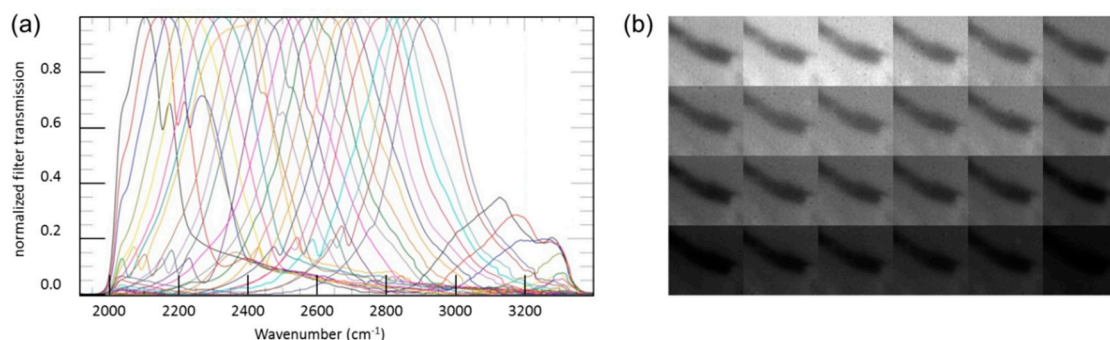
The spectral transmission of Filament filters is plotted on Figure 4a. The spectral resolution (FWHM) is about 200 cm^{-1}, much wider than the separation between filters. We can also see that the filters exhibit a secondary transmission peak at higher wavenumbers, and their extinction ratio is not zero. Nevertheless, this is not a problem for gas analysis, since the spectral transmission of the filters is fully characterized in the laboratory and could thus be considered when retrieving the data with

the radiative transfer code. The main advantage of these filters is the ease of manufacturing an array of filters with different spectral transmission, especially because all filters have the same structure, with the same layer thicknesses, the only difference being on the grating period. In the case of Filament, there are 6 × 4 filters with a 640 × 512 pixels focal plane array. Nevertheless, due to undesirable cross-talk, the final spectral image is limited to 56 × 56 pixels, by 24 spectral bands (Figure 4b).
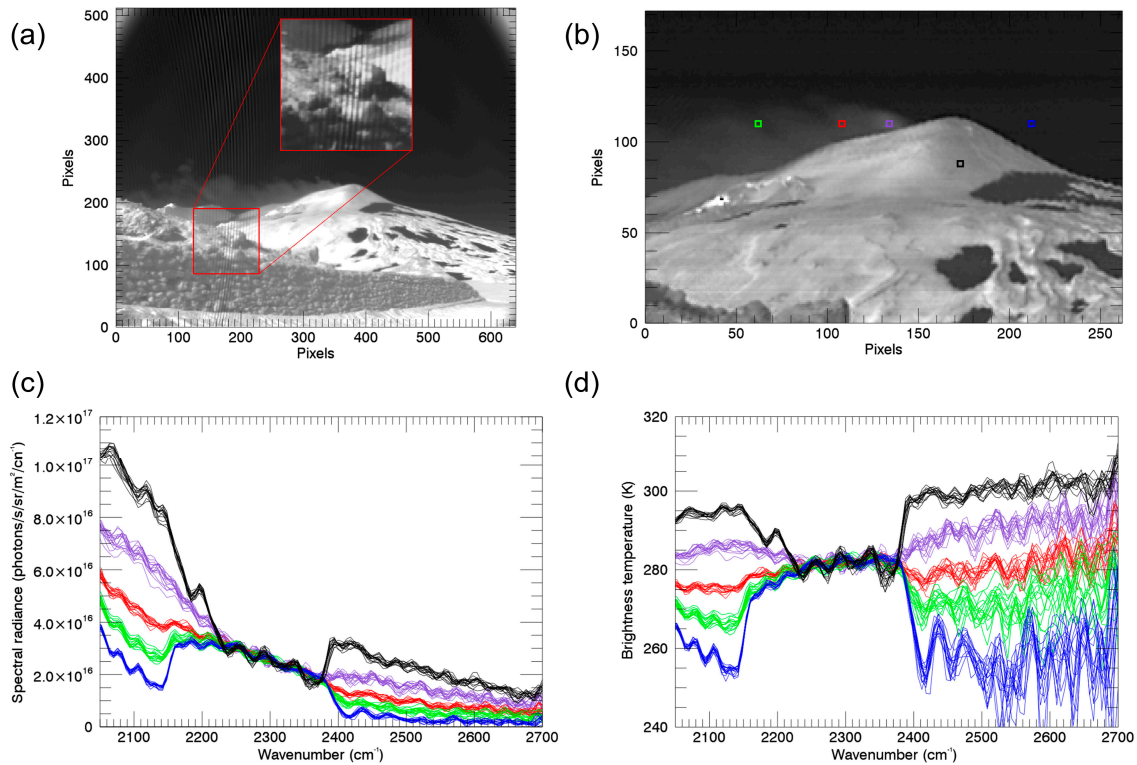
Figure 3. Spectro-Imageur Biréfringent (SIBI) measurements (**a**) Raw image (only after non-uniformity correction) showing the interference pattern superimposed on the image of the scene. A slight vignetting is also visible in the corners of the image. (**b**) Monochromatic image at 2060 cm^{-1} obtained after processing of the interferometric images. The colored dots represent areas of 4 × 4 pixels, the spectrum of these pixels being plotted below. (**c**) Spectra associated with the selected pixels on 3.b: crater surface (black), denser plume (purple), diluted plume (red and green), and clear sky (blue), measured by SIBI instrument on 25 June 2015 at 08:45. (**d**) The same spectra as on 3.c converted in brightness temperature.


Figure 4. Filament measurements (**a**) Normalized transmittance of the 24 Filament filters. (**b**) Example of the spectral images acquired for each 24 bands.

The next steps for Filament would be to correct the cross-talk between the channels by inserting an array of separation walls between the micro-lens array and the image plane. It may also be useful

for gas analysis to replace the filters by newly developed ones, with finer spectral resolution or better rejection ratio, as described by Tardieu et al. (2015) [66].

3.2. Results of Hyper-Cam LWIR

Examples of several individual spectra obtained with Hyper-Cam LWIR at different locations in the FOV of one of the sequences acquired on 26 June 2015 are presented in Figure 5. In the clear sky spectrum, the ozone signature in the spectral band 1000–1100 cm^{-1} is clearly visible (blue) and the Mt Etna is visible as a 300 K black body emission (black). By looking at different pixels in the plume (purple; orange; red; green), we can see that the greater the distance from the volcano crater, the greater the atmospheric ozone signature is detectable. Close to the crater (purple spectrum) the plume is opaque, spectral gas emission is no more detectable.
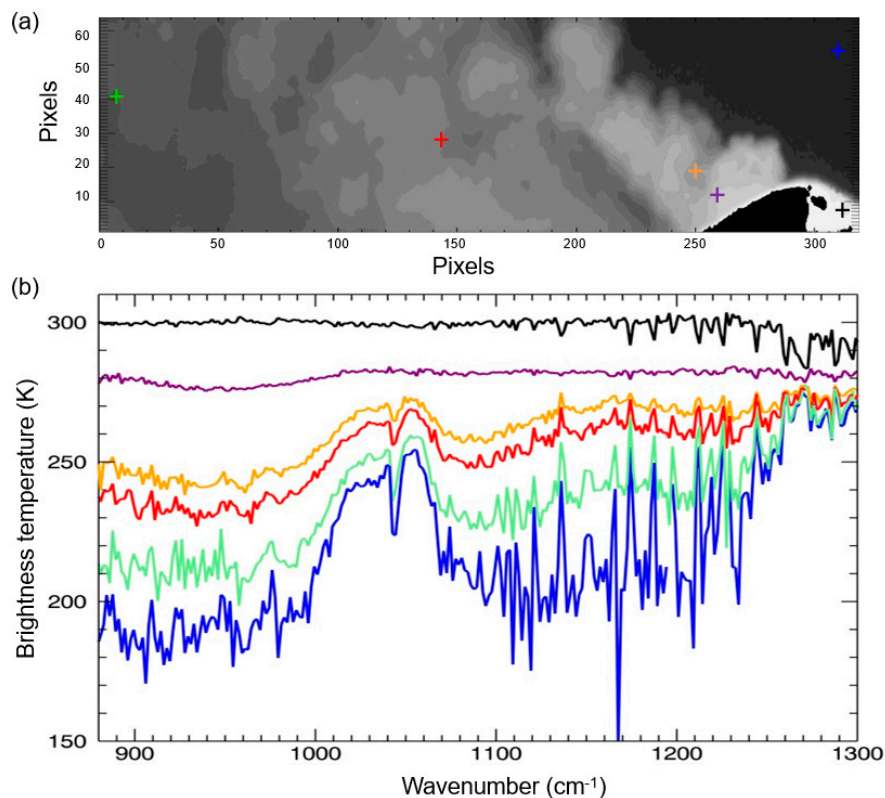

Figure 5. (**a**) Infrared image of the plume issue of Mt Etna measured by Hyper-Cam LWIR instrument on 26 June 2015 at 08:25 UTC and (**b**) brightness temperature spectrum of the selected pixels on 5.a. Crater surface (black cross), denser plume (purple and orange crosses), diluted plume (red and green crosses) and clear sky (blue cross).

3.2.1. IR Brightness Temperature Spectra: Hyper-Cam LWIR versus FTIR

As a first step, we compared FTIR OPAG 33 and Hyper-Cam LWIR brightness temperature spectra observed simultaneously in the plume. An example of a direct comparison is given in Figure 6b for diluted plume. The single pixel of FTIR instrument (blue circle in Figure 6a) is over plotted on the FOV of the Hyper-Cam LWIR sequence at 07:24 UTC on the 25 June 2015. This pixel corresponds roughly to 930 spectra collected by Hyper-Cam LWIR. A good agreement between the FTIR spectrum and the 930 mean Hyper-Cam LWIR BT spectra is observed between 880 cm^{-1} and 1310 cm^{-1}, especially in the region of O$_3$ 1000–1100 cm^{-1} as well as the one of SO$_2$ 1100–1200 cm^{-1}. The high spatial resolution of Hyper-Cam LWIR, compared to the one of the FTIR single pixel, induces a standard deviation up to 15 K. This shows the large variability of the particle and gas content in the Mt Etna plume, but also

the high sensitivity of the measurements of the Hyper-Cam LWIR instrument. Indeed, the spectral radiometric accuracy of Hyper-Cam LWIR is 0.5 K at a black body temperature of 30 °C [67].
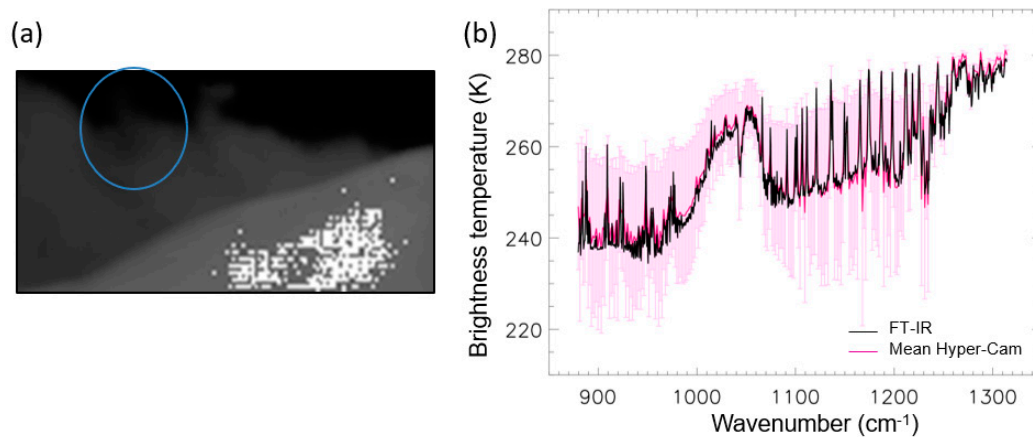

Figure 6. (**a**) Infrared image from Hyper-Cam LWIR instrument collected on 25 June 2015 at 07:24 UTC, showing Mt Etna and the volcanic plume released from North East crater. The blue circle is the area corresponding to the single pixel of the Fourier Transform InfraRed spectrometer (FTIR) OPAG 33 instrument. (**b**) Brightness temperature spectrum measured by the FTIR instrument (black), and the mean brightness temperature spectrum for the 930 Hyper-Cam LWIR pixels (pink), the error bars are the associated standard deviation corresponding to the single pixel FTIR instrument.

3.2.2. Hyper-Cam LWIR Data Retrieval

3.2.2.1. Radiance Spectra Retrieved with LARA

Examples of three radiance spectra measured and the retrieved results by LARA code for dense plume, diluted plume, and clear sky are displayed in Figure 7. Since the measurements have a spectral resolution of 2 cm^{-1} the water vapor bands are well defined and well simulated, which prevent us to attribute water vapor emission to SO$_2$ emission, or the opposite.
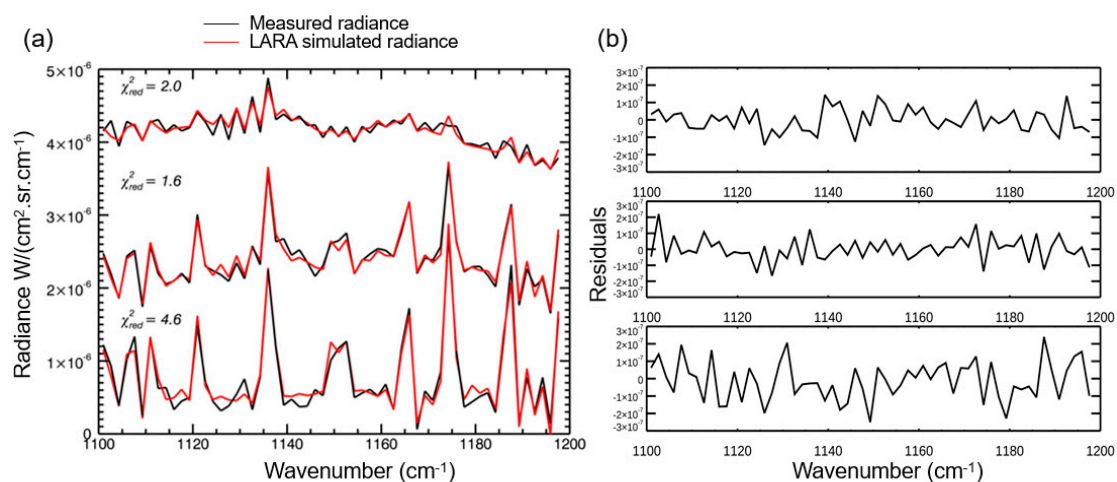

Figure 7. (**a**) Radiance spectra measured by Hyper-Cam LWIR (black) and retrieved using LARA code in the SO$_2$ spectral range 1,100–1,200 cm^{-1} on the 26 June 2015 at 08:31 UTC with a spectral resolution of 2 cm^{-1}, for three pixels: dense plume (**top**), diluted plume (**middle**) and clear sky (**bottom**). Normalized χ^2 is given for each retrieval. (**b**) Residuals of each retrieval aligned with corresponding spectrum of 7a.

A good quality of the retrievals is obtained with respectively normalized χ^2 values of 2, 1.6 and 4.6 for dense plume, diluted plume pixel, and clear sky. As a first approach, we reject retrievals with a normalized χ^2 greater than 10. This value corresponds to a mean retrieved error around 10 % on the SO_2 SCD [60].

3.2.2.2. SO_2 SCD Retrieved from Hyper-Cam LWIR Measurements

The outputs of LARA give us the slant column of SO_2 in molecules/cm^2 in the plume which are then divided by the air density to obtain the slant column density of SO_2 in ppm m. The retrievals of the spectra have been performed for each pixel independently on a computer of the AERIS data centre (www.aeris-data.fr). The full physics retrieval of one image needs roughly a week of calculation considering the configuration of the selected sequence: 320×64 pixels, spectral resolution 2 cm^{-1} and SO_2 spectral window 1,100–1,200 cm^{-1}. This large computation time must be reduced to be able to use such instrument for monitoring purposes. A pixel classification methodology is under investigation at the moment to reduce the number of retrievals. Nevertheless, a resolution reduction of the images was applied for the sensitivity tests that will be presented in the next part.

Figure 8 presents an example of SO_2 SCD (a) and normalized χ^2 (b) images obtained on the 26 June at 08:27 UTC. The selection of the pixels is made according to two threshold values: the error on the retrieved scaling factor on the SO_2 SCD calculated by the code that must be lower than 10% and a normalized $\chi^2 < 10$. The error considered here is the accuracy determined from the full covariance error matrix that includes the measurement noise and the smoothing error as described in Rodgers, 2000 [60]. The instrumental noise is equal to 5E-8 W/cm ^{2}/sr/cm^{-1}. We clearly recognize the shape of the plume. Values up to 15,000 ppm m are encountered close to the crater (right part of the image) and values in the range of 1000–4000 ppm m in the diluted part of the plume (left part of the image).
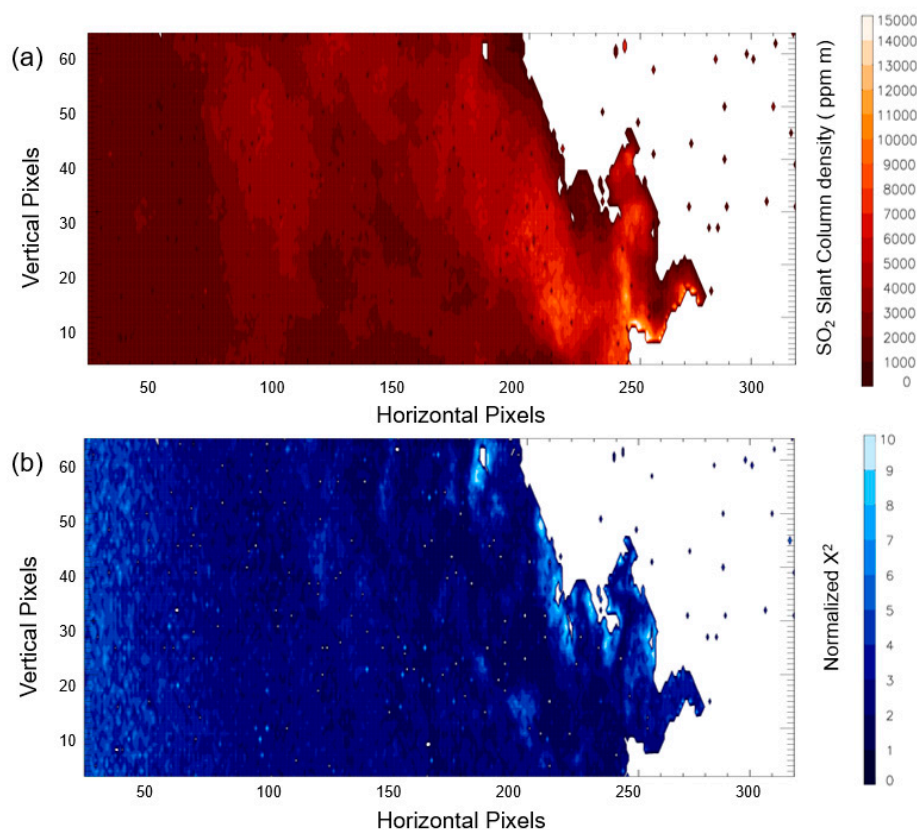
Figure 8. SO_2 Slant Column Densities (SCD) image (**a**) and normalized χ^2 image (**b**) obtained with LARA code in the spectral range 1,100–1,200 cm^{-1} on 26 June 2015 at 08:27 UTC.

Normalized χ^2 image of the plume (Figure 8b) shows that most of the spectra obtained are significantly relevant with normalized χ^2 close to 1. Very few pixels with normalized χ^2 greater than 10 exist in the plume. They probably denote emission regions perturbed by the dynamic of the plume and/or the presence of particles (water droplets, sulfate droplets, ash) which affect the IR spectra.

While the normalized χ^2 values obtained are good and the data processing is easy, the SO_2 SCD values we retrieved in dense and diluted plume regions are very high (4 to 10 times higher) compared to those previously published in the literature by measuring in the UV [16,23,68]. Such high values of SO_2 amounts were similarly encountered in the other measurement sequences of the campaign(some other examples are presented in Figure 9) To investigate the dependency of our results on the assumptions made (characteristic of plume parameters) for SO_2 SCDs retrievals, we performed sensitivity tests.
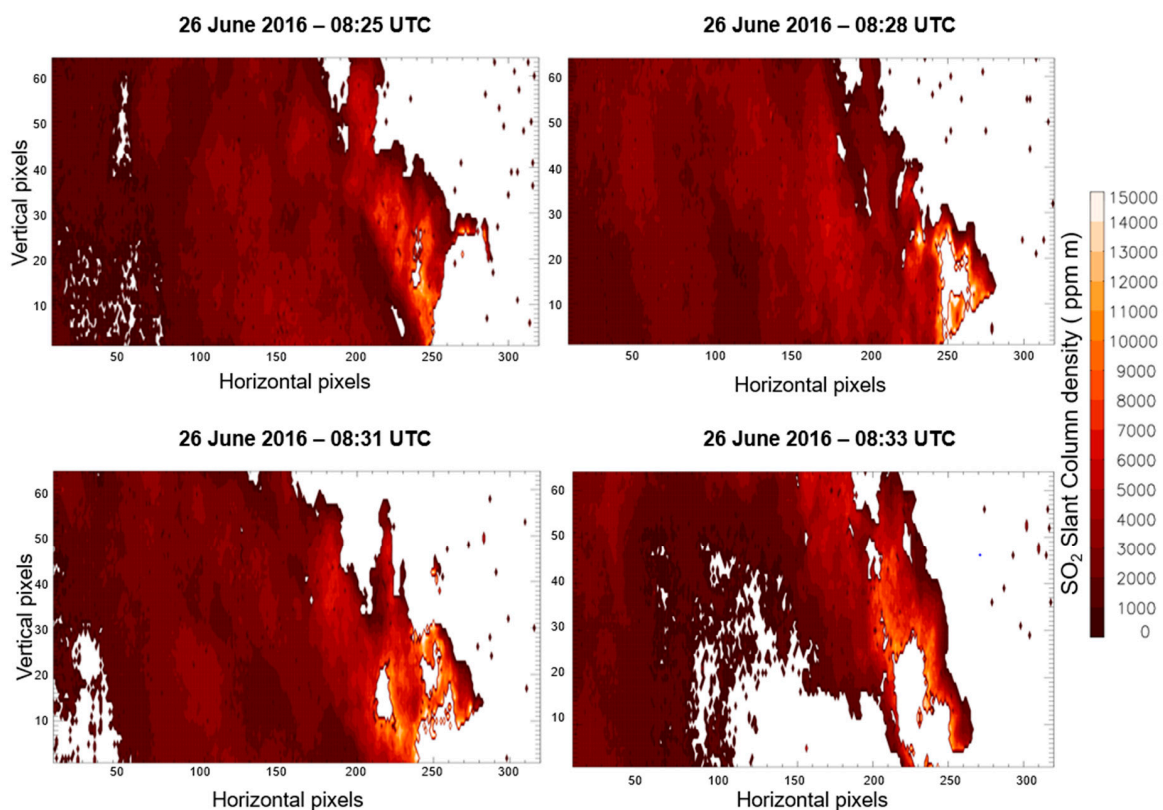
**Figure 9.** Additional SO_2 SCD images obtained from the 26 June 2015 measurement sequence.

3.2.3. Sensitivity Tests on Retrieval Parameters

Smekens and Gouhier [69] used the same instrument (Hyper-Cam LWIR) deployed at Stromboli observing a great diversity of spectra within a collected scene. They show that simple geometry cannot be applied to the entire scene with considerable variation from the top to the bottom of the image due to viewing angle. While the geometry of each pixel is considered different in our retrievals, we took assumptions on the geometry of the plume (altitude of the plume centre Z_{plume} and thickness of the plume Tk_{plume}) and on the temperature difference between the plume and the ambient air ΔT_{plume}. We tested the sensitivity of our results against these parameters. Table 2 resumes the different cases considered. For each of the nine sensitivity tests we performed, the values of two parameters were set with the reference configuration values defined in Section 2.4.2, and the third parameter was tested according to three different values presented in Table 2.

Table 2. Parameters Values Used for Sensitivity Tests in the LARA Code.

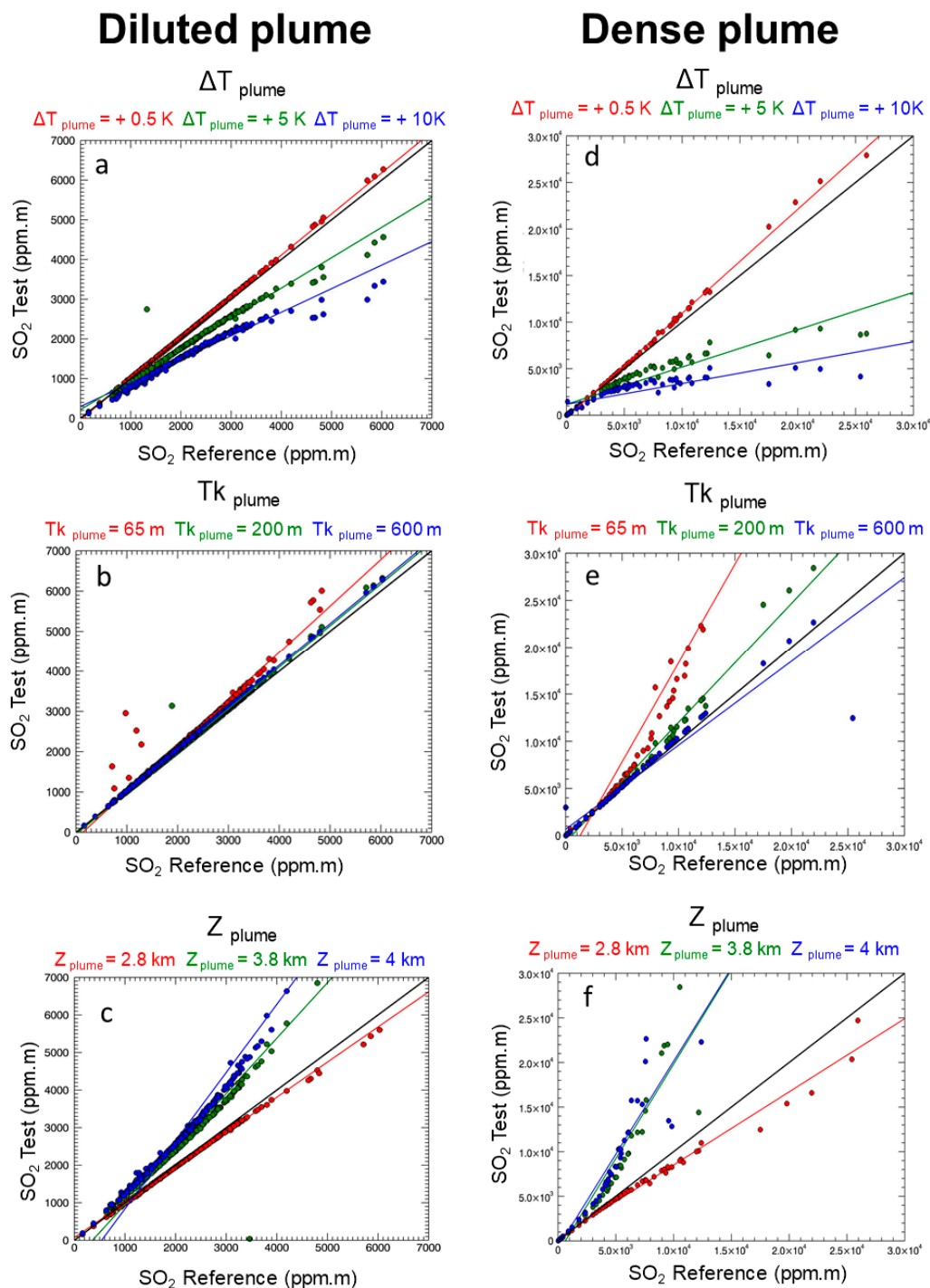| Plume Parameters	ΔT_{plume} (K) (Temperature Difference between the Plume and the Ambient Air)	Tk_{plume} (m) Plume Thickness	Z_{plume} (km) Altitude of the Plume Centre
Reference parameters values	1	400	3.2
Parameters values tested	0.5	65	2.8
	5	200	3.8
	10	600	4

As mentioned in Section 3.2.2.2, the retrieval of one image takes a significant calculation time. To minimize it for the sensitivity tests of the different parameters, we decided to reduce the number of pixels to be retrieved. We have selected one pixel out of ten for the horizontal axis and one pixel out of five for the vertical axis (Figure 10), which represent 384 pixels and a calculation time of a few hours for each tested value.
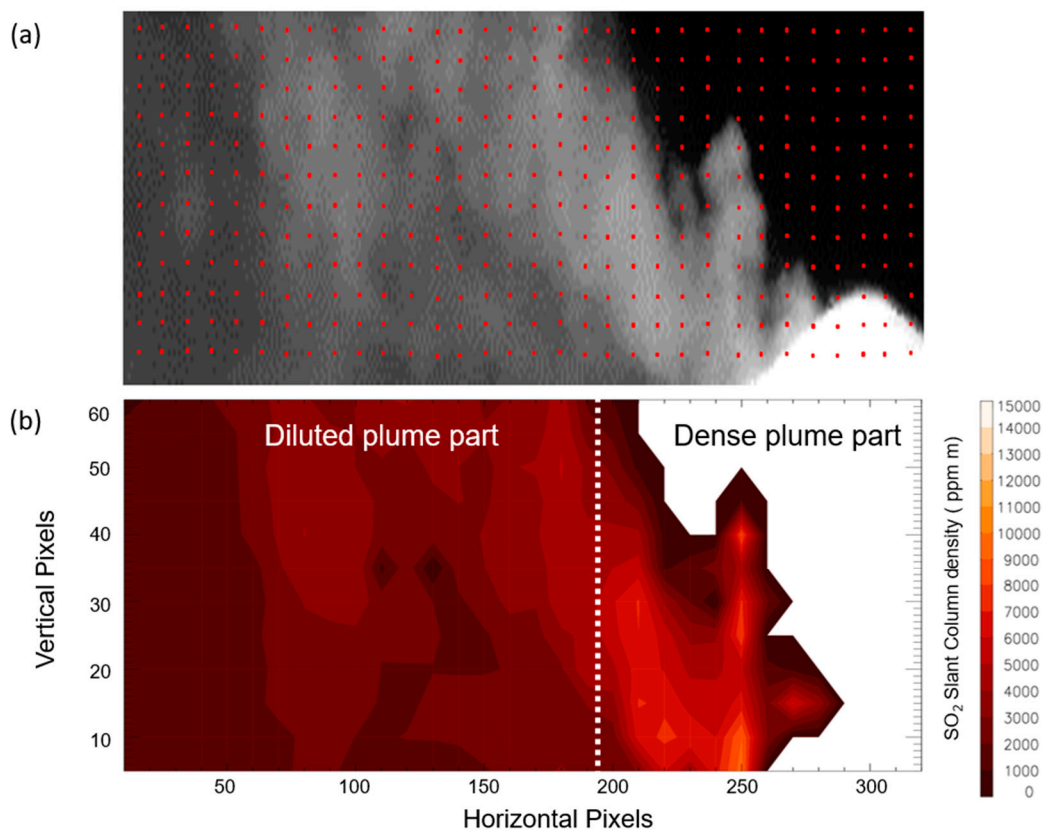
Figure 10. (**a**) Infrared image of the volcanic plume with red dots corresponding to the pixels selection (1 pixel out of five along vertical axis and one pixel out of 10 along horizontal axis). (**b**) SO$_2$ SCD image of 26 June 2016 at 08:27 UTC corresponding to the pixel selection. The white dashed line is the boundary considered between diluted plume condition (left side) and dense plume condition (right side).

For the interpretation of the results of the sensitivity tests, we chose to separate the image vertically in two parts, diluted plume part and dense plume part at horizontal pixel number 195 (white dashed line in Figure 10). The left part of the image contains normalized $\chi^2 \leq 5$ and SO$_2$ SCD values up to 7,000 ppm m (diluted plume part) whereas, the right part of the image corresponds to the dense part of the plume where SO$_2$ SCD values can attain 15,000 ppm m. The sensitivity tests correspond respectively to 225 pixels for diluted part and 65 pixels for dense part of the plume.

Figure 11 shows, for each sensitivity test, the correlation points of SO_2 SCDs for tested parameters: SO_2 SCDs for the reference. All the correlation points obtained have been fitted by a linear regression and the coefficients of determination (R^2) were calculated.

Figure 11. Sensitivity tests results on SO_2 SCD in ppm m for diluted plume (**a**–**c**) and dense plume (**d**–**f**) for the three parameters of the plume: temperature difference (**top**), plume thickness (**middle**) and altitude of the plume centre (bottom) in function of the SO_2 SCD for the reference parameters values. An ideal fit is added in black. Tests on the sequence of 26 June 2015 at 08:31 UTC.

For the diluted plume part (left part of the image), sensitivity tests on the additional temperature in the plume (Figure 11a) {0.5 K, 5 K and 10 K} give slopes of {1, 0.7 and 0.6} with very good R^2 of {0.99,

0.96 and 0.95} respectively. An additional temperature of 5 K and 10 K in the plume would decrease the SO_2 SCD by 30% and 40%, respectively. However, for the diluted plume, it would be surprising that the temperature difference reaches these values because we are far (several hundred meters) from the craters. Regarding sensitivity tests on plume thickness parameter (Figure 11b) {65 m, 200 m and 600 m} we obtain slopes of {1.1, 1 and 1} with again a very good R^2 of {0.95, 0.99 and 0.99}. Whatever the value, the slopes are close to ideal fit, so the plume thickness parameter has a small impact on SO_2 SCD for diluted plume. Sensitivity tests on the altitude of the plume centre (Figure 11c) {2.8 km, 3.8 km and 4 km} give slopes of {0.93, 1.5 and 1.8} with still very good R^2 of {0.99, 0.92 and 0.92}. For an altitude of the plume centre of 4 km we would have almost twice more SO_2 SCD than with a plume centre altitude of 3.2 km. We have very good R^2 for all the correlations in the diluted plume, a decrease of 40 % of SO_2 SCD with an additional temperature in the plume of 10 K and an increase of SO_2 SCD if the altitude of the plume centre was at 4 km.

For the dense plume part (right part of the image), sensitivity tests on the additional temperature in the plume (Figure 11d) {0.5 K, 5 K and 10 K} give slopes of {1.1, 0.4 and 0.2} with R^2 of {0.99, 0.86 and 0.67}. An additional temperature of 5 K and 10 K in the plume would decrease the SO_2 SCD by a factor of up to 2 and 6, respectively. However, the R^2 of those tests is not as good as the R^2 calculated for the diluted plume. Regarding sensitivity tests on the plume thickness parameter (Figure 11e) {65 m, 200 m and 600 m} we obtain slopes of {2.1, 1.3 and 0.9} with very good R^2 of {0.92, 0.98 and 0.9}. In opposition with the results in the diluted part, the plume thickness has a significant impact on SO_2 SCD in dense plume as a plume thickness of 65 m would double the SO_2 SCD in this part of the plume. For sensitivity tests on the altitude of the plume centre (Figure 11f) {2.8 km, 3.8 km and 4 km} we obtain slopes of {0.8, 2.1 and 2.1} with good R^2 of {0.98, 0.86 and 0.84}. As shown in the tests on diluted plume, a greater altitude of the plume centre can increase the SO_2 SCD by a factor of 2. The sensitivity of the plume parameters is significant in the dense plume retrieval of SO_2 SCD and highlights the complexity of this part of the image with the difficulty to perform a retrieval independent of the assumptions made on the plume characteristics.

The impact of plume parameters can be significant close to the crater, but it is small when we are far from the crater. The results of the sensitivity tests in the diluted plume part show the robustness of the retrieval, with a small dependency of the retrieval with respect to plume parameters and normalized χ^2 lower than 5. In the dense part of the plume we have a high dependency of the retrieval to the assumptions made on plume parameters and a higher normalized χ^2. However, it is important to notice that plume parameters used for the retrieval do not explain the high values of SO_2 SCD highlighted in the previous part.

4. Discussion

In order to investigate the SO_2 SCD retrieved by Hyper-Cam LWIR and their consistence with data reported in the literature at Mt Etna, we've compared the results obtained in the IR to those by the UV camera collected simultaneously.

UV SO_2 SCD

Figure 12 presents the image of inverted SO_2 SCD obtained by the UV camera collocated and simultaneously to the IR imager. As the UV camera has a wider FOV (28.8° × 27.9°) respect to Hyper-Cam LWIR and in order to compare the results, the UV image was cropped in relation to the IR hyperspectral imager FOV (25.6° × 5.1°). Moreover, the spatial resolution of the UV camera was also resampled to the spatial resolution of the IR imager. Along vertical axis, one pixel in the IR image corresponds to 3.5 pixels in the UV image, and along horizontal axis, one pixel in the IR image corresponds to 3.8 pixels in the UV image. We also did not consider and masked out the pixels that did not satisfy our retrieval quality conditions of the IR SO_2 SCD results.
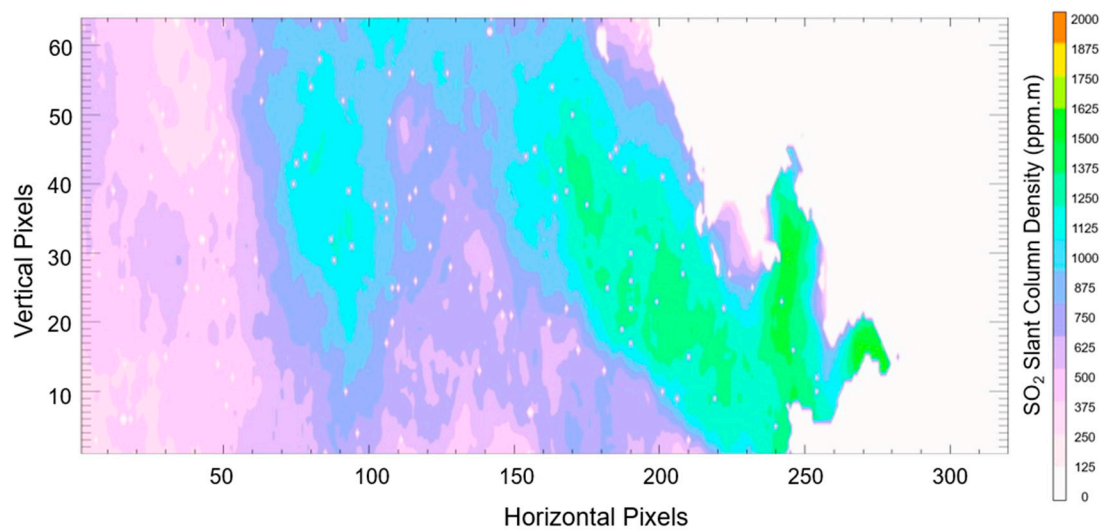
Figure 12. SO_2 SCD images measured in the UV (corresponding to Hyper-Cam LWIR field-of-view and spatial resolution) on the 26 June 2015 at 08:27 UTC at Mt Etna.

The SO_2 SCD inverted from UV images show a plume shape similar to that obtained in the IR image (previously presented in Figure 8a). It means that both instruments capture the same type of information.

The order of magnitude of the maximum values obtained by the UV camera close to the crater is ~1,500 ppm m and is ~500 ppm m in the diluted plume region. It is well known that remote observation of passive open-path SO_2 in volcanic plumes by UV spectroscopy for remote observation are affected by light dilution: not all the photons measured by the spectrometer travelled through the plume, and this effect may be very large due to in-plume scattering [70]. Unlike UV, IR is not affected by scattering.

Figure 13 shows the correlation points between SO_2 SCD in IR and SO_2 SCD in UV where two compact structures are exhibited. Indeed, as previously mentioned in 3.2.3, we consider two parts of the image, corresponding to 12,419 correlation points in the diluted part (black circles) with low SO_2 SCD values and 2,455 points in the dense part (blue circles) with high SO_2 SCD. For the diluted plume, the SO_2 SCD values are roughly in the range of 0-7,000 ppm m for the IR measurements while it corresponds to values in the range of 0-1,500 ppm m in the UV image. Since the correlation points present a compact shape it confirms that both instruments capture the same type of information in the plume. We derived a second order polynomial fit in the diluted plume (green line in Figure 13):

$$y = 1.36 \times 10^{-3}\, x^2 + 1.55x + 501.27 \tag{1}$$

where y stands for the SO_2 SCD in the IR image and x for the SO_2 SCD in the UV image. We also derived a linear fit (red line in Figure 13) to roughly give us the coefficient existing between SO_2 SCD in the IR and in the UV images. In the diluted plume the obtained slope is 3.57 with a good determination coefficient of 0.83.
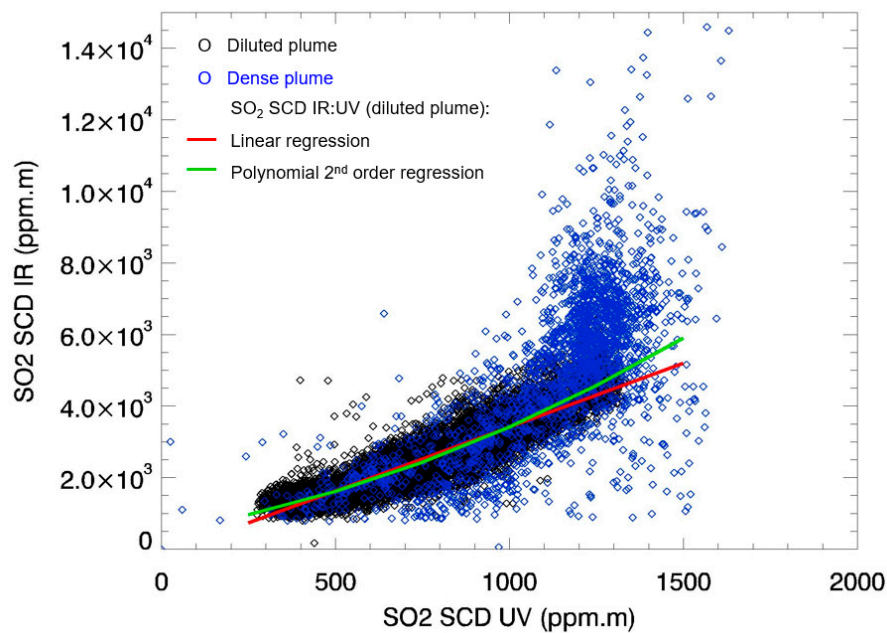
Figure 13. SO_2 SCD in the IR versus SO_2 SCD in the UV correlation points on the 26 June 2015 at 08:27 UTC at Mt Etna.

Results show that UV camera measurements roughly underestimate the SO_2 SCD by approximately a factor of 3.6 (slope of the fit).

In the region of high SO_2 SCD values, the correlation points highlight that when the IR imager measurements vary from 5,000 ppm m to 10,000 ppm m, the UV camera measurements present only low variation around 1,200 ppm m. In the dense plume, the UV camera cannot capture the variability of SO_2, which can probably be explained by light dilution.

It is very difficult to know if all of the SO_2 molecules present along the entire thickness of the plume contribute to the UV signal i.e., only the photons interacting with a partial layer of the plume contribute to the UV signal. Moreover, the UV camera measurements may be limited due to the opacity of the plume probably linked to particle concentrations, which may multiple light scattering within the plume increasing the effective path. As a result, the measured amount could either be reduced or enhanced, especially for low solar altitude angles [20,71,72]. The effective path of the UV scattered light through the plume and between the plume and the instrument can cause a significant attenuation of the measured absorbance, especially at greater distance from the plume [73–75]. Mori et al. [70] report that the larger effect of the UV scattering appears at the shorter wavelength bands and with increasing distance from a plume. The authors estimate SO_2 attenuation was not significant with any wavelength band (<±10%) at 0.6 km but was 35–50 % with shorter wavelength band at 2.6 km distance.

Kern et al. [76] performed a detailed study on the accuracy of SO_2 column densities and emission rates measured with a UV camera, by applying radiative transfer code associated with scattering effects due to aerosols. They show that taking into account scattering effects due to aerosols induces SO_2 SCD values to possibly be 1.5 or 2 times higher, and emission rates to be 20 % and 90% higher than those obtained with a conventional DOAS retrieval, depending on the different SO_2 and aerosol content present in the volcanic plume.

Smekens and Gouhier [69] show that clouds in the background could as well affect the measurements, suggesting the use of radiative transfer retrieval i.e., full physic retrievals. Our study follows this recommendation with a state vector in the SO_2 spectral range considering H_2O, CO_2, O_3, N_2O, CO, CH_4, SO_2, and plume parameters including spectral dependency of the optical thickness of the plume and considering the contribution of all these parameters to signal along the line of sight from the instrument up to 80 km.

Similarly, uncertainty exists for the IR imager measurements, whereas we parameterize particle emission to retrieved SO_2 SCD, the opacity of the dense plume could also affect the IR signal detected overestimating retrieved SO_2 SCD. The sensitivity tests we performed highlighted the complexity of the dense plume part and additional work is needed to give robust measurements of SO_2 SCD in this region. Joint explicit particle and gas radiative transfer model could be applied if the instrument could attain larger wavelength [77] to characterize the nature and the distribution of particles for dense plume.

5. Conclusions

During the IMAGETNA campaign at Mt Etna (Pizzi De Neri observatory) we have deployed three infrared imagers: SIBI, Filament and the IR hyperspectral camera Hyper-Cam LWIR from TELOPS Company. Combined with a FTIR single pixel and a UV camera we have investigated the ability of such instruments to measure SO_2 degassing from volcanic plume and to provide further constraints on the uncertainty in open-path passive UV scattering SO_2 observation.

SIBI IR imager operates in the spectral domain 3.7–4.8 μm with a spectral resolution about 14 cm^{-1}. It is easy to implement and the post processing to retrieve spectra have been performed. The limitation of SIBI during IMAGETNA campaign mainly comes from the stability of the interferometer with respect to the temperature. This could have been prevented by an in situ calibration, or a thermal control of the interferometer. Further efforts are consequently needed to evaluate its ability to use it for other gases measurements such as CO_2.

Filament infrared multispectral imager has 24 bands between 3 μm and 5 μm and uses filters leading to a spectral resolution of about 200 cm^{-1}. The next developments would be to correct the cross-talk between the channels. An option is to replace the filters to have a finer spectral resolution or a better rejection ratio, and to improve the cryogenic system in order to facilitate use during campaign.

For the first time, an IR hyperspectral camera (Hyper-Cam LWIR) has been deployed with a data processing using a line-by-line radiative transfer model to retrieve as a first step SO_2 SCD. Combined with the widely used single pixel FTIR, we have checked the radiance spectra intensity obtained by the Hyper-Cam LWIR. A good agreement was observed. The LARA line by line radiative transfer model has been applied to retrieve SO_2 SCD images from the Hyper-Cam LWIR. The SO_2 SCD obtained are higher than those reported in the literature using UV camera at Mt Etna.

The sensitivity tests on the plume characteristics assumptions highlight a limited impact on SO_2 SCD in the diluted part of the plume.

A detailed comparison of simultaneous spatial and temporal measurements from the UV camera and the IR imager have been done. Not expected very high SO_2 SCD values are obtained, with strong differences whatever the pixel considered. While the IR retrievals were easily performed with good quality (most of the normalized χ^2 are lower than five, and only a few bad pixels were detected) SO_2 SCD IR measurements are greater than SO_2 SCD UV measurements. In diluted plume condition, we have obtained a compact UV:IR correlation. This result shows that both instruments capture the same plume shape and that a polynomial correlation fit can be deduced. The UV seems to underestimate the SO_2 SCD by a factor of roughly 3.6. In the dense plume; the opacity of the plume, probably due to numerous particles, leads to a very small SO_2 SCD variability in the UV in comparison to the one in the IR. While IR measurements are less bothered by particles, this dense plume region needs to be investigated in more detail.

The light dilution in passive scattered UV remote sensing of SO_2 in volcanic plumes is complex, and mainly relies on distance between plume and instruments and aerosol burden. The quantification of effective SO_2 amounts is still an opened question. The infrared limb measurements associated with a full physic retrieval could help to quantify this phenomenon.

As a conclusion, this study highlights the potential of IR application in volcanic gas measurements at active volcanoes to investigate plume emissions all day long and that additional species can also potentially be simultaneously accessible. This study, with detailed IR and UV SO_2 measurements

comparisons, highlights the need to quantify the scattering effect on UV camera remote sensing measurements for the characterization of volcanic plume emissions.

Author Contributions: Data curation, N.H.; Formal analysis, N.H., A.P.F., L.C.; Funding acquisition, N.H.; Investigation, N.H., C.S., S.P., G.S., Y.F., D.R., S.L., A.L.S., T.C.; Methodology, S.P., G.S., Resources, S.C.; Software, C.S., S.P., G.S.; Supervision, N.H.; Visualization, C.S.; Writing – original draft, N.H.; Writing – review and editing, C.S., S.P., G.S., V.C., Y.F., T.R.

References

1. Luterbacher, J.; Pfister, C. The year without a summer. *Nat. Geosci.* **2015**, *8*, 246–248. [CrossRef]
2. Oppenheimer, C.; Fischer, T.P.; Scaillet, B. Volcanic Degassing: Process and Impact. In *Treatise on Geochemistry*, 2nd ed.; Holland, H.D., Turekian, K.K., Eds.; Elsevier Sciences: Amsterdam, The Netherlands, 2014; pp. 111–179.
3. Robock, A.; Oppenheimer, C. Volcanism and the Earth's Atmosphere. In *Geophysical Monograph Series*, 1st ed.; American Geophysical Union: Washington, DC, USA, 2003; Volume 139.
4. Wallace, P.J.; Plank, T.; Edmonds, M.; Hairu, E.H. Volatiles in Magmas. In *The Encyclopedia of Volcanoes*, 2nd ed.; Sigurdsson, H., Ed.; Academic Press: Cambridge, MA, USA, 2015; pp. 163–183.
5. Allard, P.; Carbonnelle, J.; Dajlevic, D.; Le Bronec, J.; Morel, P.; Robe, M.C.; Maurenas, J.M.; Faivre-Pierret, R.; Martin, D.; Sabroux, J.C.; et al. Eruptive and diffuse emissions of CO_2 from Mount Etna. *Nature* **1991**, *351*, 387–391. [CrossRef]
6. Bani, P.; Oppenheimer, C.; Allard, P.; Shinohara, H.; Tsanev, V.; Carn, S.; Lardy, M.; Garaebiti, E. First estimate of volcanic SO_2 budget for Vanuatu island arc. *J. Volcanol. Geoth. Res.* **2012**, *211–212*, 36–46. [CrossRef]
7. Chin, M.; Jacob, D.J. Anthropogenic and natural contributions to tropospheric sulfate: A global model analysis. *J. Geophys. Res. Atmos.* **1996**, *101*, 18691–18699. [CrossRef]
8. Graf, H.-F.; Feichter, J.; Langmann, B. Volcanic sulfur emissions: Estimates of source strength and its contribution to the global sulfate distribution. *J. Geophys. Res.* **1997**, *102*, 10727–10738. [CrossRef]
9. Stevenson, D.S.; Johnson, C.E.; Collins, W.J.; Derwent, R.G. The tropospheric sulphur cycle and the role of volcanic SO_2. *Geol. Soc.* **2003**, *213*, 295–305.
10. Minnis, P.; Harrison, E.F.; Stowe, L.L.; Gibson, G.G.; Denn, F.M.; Doelling, D.R.; Smith, W.L., Jr. Radiative Climate Forcing by the Mount Pinatubo Eruption. *Science* **1993**, *259*, 1411–1415. [CrossRef]
11. Carn, S.A.; Clarisse, L.; Prata, A.J. Multi-decadal satellite measurements of global volcanic degassing. *J. Volcanol. Geoth. Res.* **2016**, *11*, 99–134. [CrossRef]
12. Martinsson, B.G.; Brenninkmeijer, C.A.M.; Carn, S.A.; Hermann, M.; Heue, K.-P.; van Velthoven, P.F.J.; Zahn, A. Influence of the 2008 Kasatochi volcanic eruption on sulfurous and carbonaceous aerosol constituents in the lower stratosphere. *Geophys. Res. Lett.* **2009**, *36*, L12813:1–L12813:5. [CrossRef]
13. Mehta, S.K.; Fujiwara, M.; Tsuda, T.; Vernier, J.-P. Effect of recent minor volcanic eruptions on temperatures in the upper troposphere and lower stratosphere. *J. Atmos. Sol-Terr. Phys.* **2015**, *129*, 99–110. [CrossRef]
14. Sellitto, P.; Zanetel, C.; di Sarra, A.; Salerno, G.; Tapparo, A.; Meloni, D.; Pace, G.; Caltabiano, T.; Briole, P.; Legras, B. The impact of Mount Etna sulfur emissions on the atmospheric composition and aerosol properties in the central Mediterranean: A statistical analysis over the period 2000-2013 based on observations and Lagrangian modelling. *Atmos. Environ.* **2017**, *148*, 77–88. [CrossRef]
15. Edmonds, M. New geochemical insights into volcanic degassing. *Philos. T. R. Soc. A* **2008**, *366*, 4559–4579. [CrossRef]

16. Salerno, G.G.; Burton, M.; Di Grazia, G.; Caltabiano, T.; Oppenheimer, C. Coupling between Magmatic Degassing and Volcanic Tremor in Basaltic Volcanism. *Front. Earth Sci.* **2018**, *6*, 157:1–157:12.

17. Sutton, A.J.; Elias, T.; Gerlach, T.M.; Stokes, J.B. Implications for eruptive processes as indicated by sulfur dioxide emission from Kïlauea volcano, Hawaii, USA, 1979-1997. *J. Volcanol. Geoth. Res.* **2001**, *108*, 283–302. [CrossRef]

18. Caltabiano, T.; Burton, M.; Giammanco, S.; Allard, P.; Bruno, N.; Muré, F.; Romano, R. Volcanic Gas Emissions from the Summit Craters and Flanks of Mt. Etna, 1987–2000. *Geophy. Monog. Ser.* **2004**, *143*, 111–128.

19. Galle, B.; Johansson, M.; Rivera, C.; Zhang, Y.; Kihlman, M.; Kern, C.; Lehmann, T.; Platt, U.; Arellano, S.; Hidalgo, S. Network for Observation of Volcanic and Atmospheric Change (NOVAC)—A global network for volcanic gas monitoring: Network layout and instrument description. *J. Geophys. Res. Atmos.* **2010**, *115*, D05304:1–D05304:19. [CrossRef]

20. Hamilton, P.M.; Varey, R.H.; Millán, M.M. Remote sensing of sulphur dioxide. *Atmos. Environ.* **1978**, *12*, 127–133. [CrossRef]

21. Manatt, S.L.; Lane, A.L. A compilation of the absorption cross-section of SO_2 from 106 to 403 nm. *J. Quant. Spectrosc. Radiat. Transf.* **1993**, *50*, 267–276. [CrossRef]

22. Allard, P.; Carbonnelle, J.; Métrich, N.; Loyer, H.; Zettwoog, P. Sulphur output and magma degassing budget of Stromboli volcano. *Nature* **1994**, *368*, 326–330. [CrossRef]

23. Williams-Jones, G.; Stix, J.; Hickson, C. The COSPEC Cookbook: Making SO2 Measurements at Active Volcanoes. In *Methods in Volcanology 1*; IAVCEI: Rome, Italy, 2008.

24. Newcomb, G.S.; Millan, M.M. Theory, Applications, and Results of the Long-Line Correlation Spectrometer. *IEEE T. Geosci. Electron.* **1970**, *8*, 149–157. [CrossRef]

25. Stoiber, R.E.; Malinconico, L.L.; Williams, S.N. Use of the correlation spectrometer at volcanoes. In *Volcanic Events*; Tazieff, H., Sabroux, J.C., Eds.; Elsevier: Amsterdam, The Netherlands, 1983; Volume 1, pp. 424–444.

26. Salerno, G.G.; Burton, M.R.; Oppenheimer, C.; Caltabiano, T.; Tsanev, V.I.; Bruno, N. Novel retrieval of volcanic SO_2 abundance from ultraviolet spectra. *J. Volcanol. Geoth. Res.* **2009**, *181*, 141–153. [CrossRef]

27. Bluth, G.J.S.; Shannon, J.M.; Watson, I.M.; Prata, A.J.; Realmuto, V.J. Development of an ultra-violet digital camera for volcanic SO_2 imaging. *J. Volcanol. Geoth. Res.* **2007**, *161*, 47–56. [CrossRef]

28. Mori, T.; Burton, M. The SO_2 camera: A simple, fast and cheap method for ground-based imaging of SO_2 in volcanic plumes. *Geophys. Res. Lett.* **2006**, *33*, L24804:1–L24804:5. [CrossRef]

29. Platt, U.; Lübcke, P.; Kuhn, J.; Bobrowski, N.; Prata, F.; Burton, M.; Kern, C. Quantitative imaging of volcanic plumes—Results, needs, and future trends. *J. Volcanol. Geoth. Res.* **2015**, *300*, 7–21. [CrossRef]

30. Francis, P.; Burton, M.; Oppenheimer, C. Remote measurements of volcanic gas compositions by solar occultation spectroscopy. *Nature* **1998**, *396*, 567–570. [CrossRef]

31. Love, S.P.; Goff, F.; Counce, D.; Siebe, C.; Delgado, H. Passive infrared spectroscopy of the eruption plume at Popocatepetl volcano, Mexico. *Nature* **1998**, *396*, 563–567. [CrossRef]

32. La Spina, A.; Burton, M.; Salerno, G.G. Unravelling the processes controlling gas emissions from the central and northest craters of Mt Etna. *J. Volcanol. Geoth. Res.* **2010**, *198*, 368–376. [CrossRef]

33. Notsu, K.; Mori, T.; Igarashi, G.; Tohjima, Y.; Wakita, H. Infrared spectral radiometer: A new tool for remote measurement of SO_2 of volcanic gas. *Geochem. J.* **1993**, *27*, 361–366. [CrossRef]

34. Prata, A.J.; Bernardo, C. Retrieval of volcanic ash particle size, mass and optical depth from a ground-based thermal infrared camera. *J. Volcanol. Geoth. Res.* **2009**, *186*, 91–107. [CrossRef]

35. Allard, P.; Burton, M.; Muré, F. Spectroscopic evidence for a lava fountain driven by previously accumulated magmatic gas. *Nature* **2005**, *433*, 407–410. [CrossRef]

36. La Spina, A.; Burton, M.; Allard, P.; Alparone, S.; Muré, F. Open-path FTIR spectroscopy of magma degassing processes during eight lava fountains on Mount Etna. *Earth Planet. Sc. Lett.* **2015**, *413*, 123–134. [CrossRef]

37. Thomas, H.E.; Watson, I.M. Observations of volcanic emissions from space: current and future perspectives. *Nat. Hazards* **2010**, *54*, 323–354. [CrossRef]

38. Theys, N.; Campion, R.; Clarisse, L.; Brenot, H.; van Gent, J.; Dils, B.; Corradini, S.; Merucci, L.; Coheur, P.-F.; Van Roozendael, M.; et al. Volcanic SO_2 fluxes derived from satellite data: a survey using OMI, COME-2, IASI and MODIS. *Atmos. Chem. Phys.* **2013**, *13*, 5945–5968. [CrossRef]

39. Prata, A.J.; Bernardo, C. Retrieval of sulfur dioxide from a ground-based thermal infrared imaging camera. *Atmos. Meas. Tech.* **2014**, *7*, 2807–2828. [CrossRef]

40. Gabrieli, A.; Porter, J.N.; Wright, R.; and Lucey, P.G. Validating the accuracy of SO_2 gas retrievals in the thermal infrared (8-14 μm). *Bull. Volcanol.* **2017**, *79*, 80:1–80:18. [CrossRef]

41. Briottet, X.; Boucher, Y.; Dimmeler, A.; Malaplate, A.; Cini, A.; Diani, M.; Bekman, H.; Scwering, P.; Skauli, T.; Kasen, I.; et al. Military applications of hyperspectral imagery. In Proceedings of the Targets and Backgrounds XII: Characterization and Representation, Defense and Security Symposium, Orlando (Kissimmee), FL, USA, 17–21 April 2006; Volume 6239, pp. 62390B:1–62390B:8.

42. Friedl-Vallon, F.; Riese, M.; Maucher, G.; Lengel, A.; Hase, F.; Preusse, P.; Spang, R. Instrument concept and preliminary performance analysis of GLORIA. *Adv. Space Res.* **2006**, *37*, 2287–2291. [CrossRef]

43. Riese, M.; Oelhaf, H.; Preusse, P.; Blank, J.; Ern, M.; Friedl-Vallon, F.; Fischer, H.; Guggenmoser, T.; Höpfner, M.; Hoor, P.; et al. Gimballed Limb Observer for Radiance Imaging of the Atmosphere (GLORIA) scientific objectives. *Atmos. Meas. Tech.* **2014**, *7*, 1915–1928. [CrossRef]

44. Ungermann, J.; Kaufmann, M.; Hoffmann, L.; Preusse, P.; Oelhaf, H.; Friedl-Vallon, F.; Riese, M. Towards a 3-D tomographic retrieval for the air-borne limb-imager GLORIA. *Atmos. Meas. Tech.* **2010**, *3*, 1647–1665. [CrossRef]

45. Pola Fossi, A.; Ferrec, Y.; Roux, N.; D'almeida, O.; Guerineau, N.; Sauer, H. Miniature and cooled hyperspectral camera for outdoor surveillance applications in the mid-infrared. *Opt. Lett.* **2016**, *41*, 1901–1904. [CrossRef]

46. Sakat, E.; Vincent, G.; Rommeluère, S.; Eradès, C.; Lefebvre, S.; Cauty, F.; Collin, S.; Druart, G.; Pelouard, J.-L.; Haïdar, R. Analysis of propellant combustion with real-time multispectral infrared camera. In Proceedings of the Infrared Technology and Applications XXXIX, International Society for Optics and Photonics, SPIE Defense Security and Sensing, Baltimore, ML, USA, 29 April–3 May 2013; Volume 8704, pp. 87042R:1–87042R:5.

47. Tremblay, P.; Savary, S.; Rolland, M.; Villemaire, A.; Chamberland, M.; Farley, V.; Brault, L.; Giroux, J.; Allard, J.-L.; Dupuis, E.; et al. Standoff gas identification and quantification from turbulent stack plumes with an imaging Fourier-transform spectrometer. In Proceedings of the Advanced Environmental, Chemical, and Biological Sensing Technologies VII, SPIE Defense Security and Sensing, Orlando, FL, USA, 5–9 April 2010; Volume 7673, pp. 76730H:1–76730H:12.

48. Ferrec, Y. Spectro-imagerie aéroportée par transformation de Fourier avec un interféromètre statique à décalage latéral: réalisation et mise en oeuvre. Ph.D. Thesis, Université Paris Sud, Paris, France, 2008.

49. Davis, S.; Abrams, M.; Brault, J. *Fourier Transform Spectrometry*; Elsevier: Cambridge, MA, USA, 2001; p. 262.

50. Pola Fossi, A. Miniaturisation d'une caméra hyperspectrale infrarouge. Ph.D. Thesis, Office National d'Etudes et de Recherches Aérospatiales, Université Paris, Palaiseau, France, 2016.

51. Shogenji, R.; Kitamura, Y.; Yamada, K.; Miyatake, S.; Tanida, J. Multispectral imaging using compact compound optics. *Opt. Express* **2004**, *12*, 1643–1655. [CrossRef]

52. Sakat, E.; Vincent, G.; Ghenuche, P.; Bardou, N.; Dupuis, C.; Collin, S.; Pardo, F.; Haïdar, R.; Pelouard, J.-L. Free-standing guided-mode resonance band-pass filters: from 1D to 2D structures. *Opt. Express* **2012**, *20*, 13082–13090. [CrossRef] [PubMed]

53. Payan, S.; Camy-Peyret, C.; Jeseck, P.; Hawat, T.; Durry, G.; Lefèvre, F. First direct simultaneous HCl and ClONO2 profile measurements in the Arctic Vortex. *Geophys. Res. Lett.* **1998**, *25*, 2663–2666. [CrossRef]

54. Payan, S.; Camy-Peyret, C.; Bureau, J. Comparison of Retrieved L2 Products from Four Successive Versions of L1B Spectra in the Thermal Infrared Band of TANSO-FTS over the Arctic Ocean. *Remote Sens.* **2017**, *9*, 1167. [CrossRef]

55. Butz, A.; Bösch, H.; Camy-Peyret, C.; Dorf, M.; Engel, A.; Payan, S.; Pfeilsticker, K. Observational constraints on the kinetics of the ClO-BrO and ClO-ClO ozone loss cycles in the Arctic winter stratosphere. *Geophys. Res. Lett.* **2007**, *34*, L05801:1–L05801:5. [CrossRef]

56. Mondelain, D.; Payan, S.; Deng, W.; Camy-Peyret, C.; Hurtmans, D.; Mantz, A.W. Measurement of the temperature dependence of line mixing and pressure broadening parameters between 296 and 90 K in the ν3 band of $^{12}CH_4$ and their influence on atmospheric methane retrievals. *J. Mol. Spectrosc.* **2007**, *244*, 130–137. [CrossRef]

57. Payan, S.; Camy-Peyret, C.; Oelhaf, H.; Wetzel, G.; Maucher, G.; Keim, C.; Pirre, M.; Huret, N.; Engel, A.; Volk, M.C.; et al. Validation of version-4.61 methane and nitrous oxide observed by MIPAS. *Atmos. Chem. Phys.* **2009**, *9*, 413–442. [CrossRef]

58. Keim, C.; Eremenko, M.; Orphal, J.; Dufour, G.; Flaud, J.-M.; Höpfner, M.; Boynard, A.; Clerbaux, C.; Payan, S.; Coheur, P.-F.; et al. Tropospheric ozone from IASI: Comparison of different inversion algorithms and validation with ozone sondes in the northern middle latitudes. *Atmos. Chem. Phys.* **2009**, *9*, 9329–9347. [CrossRef]

59. Razavi, A.; Clerbaux, C.; Wespes, C.; Clarisse, L.; Hurtmans, D.; Payan, S.; Camy-Perret, C.; Coheur, P.-F. Characterization of methane retrievals from the IASI space-borne sounder. *Atmos. Chem. Phys.* **2009**, *9*, 7889–7899. [CrossRef]

60. Rodgers, C.D. *Inverse Methods for Atmospheric Sounding: Theory and Practice*; World Scientific: Singapore, 2000.

61. Rothman, L.S.; Gordon, I.E.; Babikov, Y.; Barbe, A.; Chris Benner, D.; Bernath, P.F.; Birk, M.; Bizzocchi, L.; Boudon, V.; Brown, L.R.; et al. The HITRAN2012 molecular spectroscopic database. *J. Quant. Spectrosc. Radiat. Transf.* **2013**, *130*, 4–50. [CrossRef]

62. Clough, S.A.; Shephard, M.W.; Mlawer, E.J.; Delamere, J.S.; Iacono, M.J.; Cady-Pereira, K.; Boukabara, S.; Brown, P.D. Atmospheric radiative transfer modeling: a summary of the AER codes. *J. Quant. Spectrosc. Radiat. Transf.* **2005**, *91*, 233–244. [CrossRef]

63. Rix, M.; Valks, P.; Hao, N.; van Geffen, J.; Clerbaux, C.; Clarisse, L.; Coheur, P.-F.; Loyala, R.D.G.; Erbertseder, T.; Zimmer, W.; et al. Satellite monitoring of volcanic sulfur dioxide emissions for early warning of volcanic hazards. *IEEE J. Sel. Top. Appl. Earth Obs. Remote Sens.* **2009**, *2*, 196–206. [CrossRef]

64. Burton, M.R.; Prata, F.; Platt, U. Volcanological applications of SO_2 cameras. *J. Volcanol. Geoth. Res.* **2015**, *200*, 2–5. [CrossRef]

65. Platt, U.; Stutz, J. *Differential Optical Absorption Spectroscopy, Principles and Applications, Series: Physics of Earth and Space Environments*; Springer: Berlin/Heidelberg, Germany, 2008.

66. Tardieu, C.; Estruch, T.; Vincent, G.; Jaeck, J.; Bardou, N.; Collin, S.; Haïdar, R. Extraordinary optical extinctions through dual metallic gratings. *Opt. Lett.* **2015**, *40*, 661–664. [CrossRef] [PubMed]

67. Lagueux, P.; Farleu, V.; Chamberland, M.; Villemaire, A.; Turcotte, C.; Puckrin, E. Design and Performance of the Hyper-Cam, an Infrared Hyperspectral Imaging Sensor. 2009. Available online: https://pdfs.semanticscholar.org/2f75/90496d218177bd059fe6bbab98ad69afc36e.pdf (accessed on 11 May 2019).

68. D'Aleo, R.; Bitetto, M.; Delle Donne, D.; Tamburello, G.; Battaglia, A.; Coltelli, M.; Patanè, D.; Prestifilippo, M.; Sciotto, M.; Aiuppa, A. Spatially resolved SO_2 flux emissions from Mt Etna. *Geophys. Res. Lett.* **2016**, *43*, 7511–7519.

69. Smekens, J.F.; Gouhier, M. Observation of SO_2 degassing at Stromboli volcano using a hyperspectral thermal infrared imager. *J. Volcanol. Geoth. Res.* **2018**, *356*, 75–89. [CrossRef]

70. Mori, T.; Mori, T.; Kazahaya, K.; Ohwada, M.; Hirabayashi, J.; Yoshikawa, S. Effect of UV scattering on SO2 emission rate measurements. *Geophys. Res. Lett.* **2006**, *33*, L17315:1–L17315:5. [CrossRef]

71. Edner, H.; Ragnarson, P.; Svanberg, S.; Wallinder, E.; Ferrara, R.; Cioni, R.; Raco, B.; Taddeucci, G. Total fluxes of sulfur dioxide from the Italian volcanoes Etna, Stromboli, and Vulcano measured by differential absorption lidar and passive differential optical absorption spectroscopy. *J. Geophys. Res. Atmos.* **1994**, *99*, 18827–18838. [CrossRef]

72. Weibring, P.; Swartling, J.; Edner, H.; Svanberg, S.; Caltabiano, T.; Condarelli, D.; Cecchi, G.; Pantani, L. Optical monitoring of volcanic sulphur dioxide emissions – comparison between four different remote-sensing spectroscopic techniques. *Opt. Laser Eng.* **2002**, *37*, 267–284. [CrossRef]

73. Moffat, A.J.; Millan, M.M. The applications of optical correlation techniques to the remote sensing of SO2 plumes using sky light. *Atmos. Environ.* **1971**, *5*, 677–690. [CrossRef]

74. Millán, M.M. Remote sensing of air pollutants. A study of some atmospheric scattering effects. *Atmos. Environ.* **1980**, *14*, 1241–1253.

75. Hoff, R.M. Differential SO_2 column measurements of the Mt. Pinatubo volcanic plume. *Geophys. Res. Lett.* **1992**, *19*, 175–178. [CrossRef]

76. Kern, C.; Deutschmann, T.; Werner, C.; Sutton, A.J.; Elias, T.; Kelly, P.J. Improving the accuracy of SO_2 column densities and emission rates obtained from upward-looking UV-spectroscopic measurements of volcanic plumes by taking realistic radiative transfer into account. *J. Geophys. Res. Atmos.* **2012**, *117*, D20302:1–D20302:23. [CrossRef]

77. Dubuisson, P.; Herbin, H.; Minvielle, F.; Compiègne, M.; Thieuleux, F.; Parol, F.; and Pelon, J. Remote sensing of volcanic ash plumes from thermal infrared: A case study analysis from SEVIRI, MODIS and IASI instruments. *Atmos. Meas. Tech.* **2014**, *7*, 359–371. [CrossRef]